Neck configuration of Cm and Cf nuclei in the fission state within the relativistic mean field formalism

M. Bhuyan,[1,2,*] B. V. Carlson,[3,†] S. K. Patra,[4,‡] and Raj K. Gupta[5]

[1]*Department of Physics, Faculty of Science, University of Malaya, Kuala Lumpur 50603, Malaysia*
[2]*Institute of Research and Development, Duy Tan University, Da Nang 550000, Vietnam*
[3]*Instituto Tecnológico de Aeronáutica, São José dos Campos 12.228-900, São Paulo, Brazil*
[4]*Institute of Physics, Sachivalaya Marg, Sainik School, Bhubaneswar 751005, India*
[5]*Department of Physics, Panjab University, Chandigarh, Punjab 160014, India*

(Received 21 June 2019; published 8 November 2019)

A correlation is established between the neutron multiplicity and the neutron number in the fission state of curium and californium isotopes within a microscopic study using relativistic mean field formalism. The study includes the isotopes of Cm and Cf nuclei near the valley of stability, and hence is likely to play an important role in the artificial synthesis of superheavy nuclei. The static fission path, the evolution of the neck, the neutron-proton asymmetry of the neck, and its composition in terms of nucleon numbers are also estimated. We find a maximum ratio for average neutron to proton density, which is about 1.6 in the breakdown of the liquid-drop picture for ^{248}Cm and ^{252}Cf. A strong dependence of the neutron-proton asymmetry on the neutron multiplicity in an isotopic chain is also observed. The present work suggests a breakdown of the liquid-drop picture of the parent nucleus into two heavy fragments along with an α particle at scission point for ^{242,244,246,248}Cm and ^{248,250,252,254}Cf.

DOI: 10.1103/PhysRevC.100.054312

I. INTRODUCTION

The first interpretation of nuclear fission was made about eight decades ago, though many features of this process are still in the rudimentary stage. The discovery of nuclear fission [1] was recognized as an evolution of the nuclear shape from a single compound nucleus split into two receding fragments [2,3]. This conceptual framework within the macroscopic-microscopic approach to the calculation of nuclear binding energies, provides a powerful theoretical tool for studies of low-energy fission dynamics. Further analysis from the microscopic theories to exploration of its dynamics are also prime objectives at present in nuclear physics. To explain the fission properties of superheavy nuclei, it is essential to measure the shape (i.e., height and width) of the barriers and shape degrees of freedom [3–8]. In early days, the fission shapes were investigated by minimizing the sum of the Coulomb and surface energies using a development of the radius in the liquid-drop model (LDM). Recently, fusion studies have shown that the effects of the nuclear forces in the neck region (i.e., the gap between two fragments) of the deformed valley are indeed needed for optimizing the proximity energy of the fission process. The goal is more or less reached by following the studies from the macroscopic-microscopic (*mic-mac*) model [9–14], the extended Thomas-Fermi with Strutinsky integral (ETFSI) method [15,16], nonrelativistic Skyrme-Hartree-Fock [17–22], Gogny force [23–26], and relativistic mean field models [27–35].

The use of the adiabatic approximation in the fission process is an interpretation of the potential energy surface (PES), an analog of the classical phase space of Lagrangian and Hamiltonian mechanics. The fission point of a nucleus can be determined from the total nuclear potential energy as a function of the shape coordinates relative to the ground state of the most favorable saddle point where the configuration evolves from a single nucleus into two separated fragments. The current way to deal with the splitting fragments depends on the most relevant collective variables of the nuclear shape, such as elongation, reflection asymmetry, and neck structure that can be described by the multipolarity deformations [24,33,34,36]. Furthermore a critical feature of the fission process is the multiplicity of neutron and/or small $N = Z$ nuclei from the two fragments at the postscission point after they are accelerated by the mutual Coulomb repulsion [29,37–39]. In this process, the neck is believed to be neutron rich and favorable for neutron emission rather than proton and/or α-particle emission. At present, it is not possible to ascertain the true composition of the neck experimentally, which has the potential to reveal many important aspects of the fission dynamics.

The PES spanned by the relevant degrees of freedom of a fissile nucleus can be used to reveal a static fission path, fission lifetime, mass of the fragments and also many features of fission dynamics [26,29,33–36,40–42]. To generate the neck structure of actinide nuclei and to determine

*bunuphy@um.edu.my
†brettvc@gmail.com
‡patra@iopb.res.in

the constituents of the neck (i.e., the average neutron-proton asymmetry and the neutron multiplicity) quantitatively, can be used to benchmark the predictive power of theoretical models [26,29,30,33,34,37,43,44]. Such a study would be a step forward in the understanding of the fission dynamics of actinide nuclei [29,33,35] and the synthesis process in the experimental laboratories available at present and/or under construction around the world [45–53]. Further the composition of the neck in the fission state of actinide nuclei may involve information regarding the formation of the elements in the rapid neutron capture process (i.e., r process) of nuclear synthesis in stellar evolution [54–56]. In the present study we examine the properties of the fission state of actinides using the axially deformed relativistic mean field model.

This paper is organized as follows: In Sec. II we outline the relativistic mean field approach involved in the calculations. The calculations and results are given in Sec. III. Finally, a brief summary and conclusions are given in Sec. IV.

II. THEORETICAL FORMALISMS

The microscopic self-consistent mean field calculation is one of the standard tools to investigate the properties of infinite nuclear matter and nuclear structure phenomena [17,18,21,22,26,33–35,40–42,57–59]. The relativistic mean field (RMF) approach is one of the most popular and widely used formalisms among them. It starts with a basic Lagrangian that describes nucleons as Dirac spinors interacting through different meson fields. The relativistic mean field Lagrangian density, which has several modifications to account for various limitations of the Walecka Lagrangian [57,58] for a nucleon-meson many-body system [57–76], is

$$\begin{aligned}\mathcal{L} = {} & \overline{\psi}\{i\gamma^{\mu}\partial_{\mu} - M\}\psi + \frac{1}{2}\partial^{\mu}\sigma\,\partial_{\mu}\sigma \\ & - \frac{1}{2}m_{\sigma}^{2}\sigma^{2} - \frac{1}{3}g_{2}\sigma^{3} - \frac{1}{4}g_{3}\sigma^{4} - g_{s}\overline{\psi}\psi\sigma \\ & - \frac{1}{4}\Omega^{\mu\nu}\Omega_{\mu\nu} + \frac{1}{2}m_{w}^{2}\omega^{\mu}\omega_{\mu} - g_{w}\overline{\psi}\gamma^{\mu}\psi\omega_{\mu} \\ & - \frac{1}{4}\vec{B}^{\mu\nu}.\vec{B}_{\mu\nu} + \frac{1}{2}m_{\rho}^{2}\vec{\rho}^{\mu}.\vec{\rho}_{\mu} - g_{\rho}\overline{\psi}\gamma^{\mu}\vec{\tau}\psi\cdot\vec{\rho}^{\mu} \\ & - \frac{1}{4}F^{\mu\nu}F_{\mu\nu} - e\overline{\psi}\gamma^{\mu}\frac{(1-\tau_{3})}{2}\psi A_{\mu}. \end{aligned} \tag{1}$$

The ψ is the Dirac spinor for the nucleon whose third component of isospin is denoted by τ_3. Here g_σ, g_ω, g_ρ, and $\frac{e^2}{4\pi}$ are the coupling constants for the σ, ω, ρ meson and photon, respectively. The constant g_2 and g_3 are for the self-interacting nonlinear σ-meson field. The masses of the σ, ω, ρ mesons and nucleons are m_σ, m_ω, m_ρ, and M, respectively. The quantity A_μ stands for the electromagnetic field. The vector field tensors for the ω^μ, $\vec{\rho}_\mu$ and photon are given by

$$F^{\mu\nu} = \partial_{\mu}A_{\nu} - \partial_{\nu}A_{\mu}, \tag{2}$$

$$\Omega_{\mu\nu} = \partial_{\mu}\omega_{\nu} - \partial_{\nu}\omega_{\mu}, \tag{3}$$

and

$$\vec{B}^{\mu\nu} = \partial_{\mu}\vec{\rho}_{\nu} - \partial_{\nu}\vec{\rho}_{\mu}, \tag{4}$$

respectively. From the above Lagrangian, we obtain the field equations for the nucleons and mesons. These equations are solved by expanding the upper and lower components of the Dirac spinors and the boson fields in an axially deformed harmonic oscillator basis, with an initial deformation β_0. The set of coupled equations are solved numerically by a self-consistent iteration method [44,77–79]. The center-of-mass motion energy correction is estimated by the harmonic oscillator formula $E_{\text{c.m.}} = \frac{3}{4}(41A^{-1/3})$. The quadrupole deformation parameter β_2 is evaluated from the resulting proton and neutron quadrupole moments, as

$$Q = Q_n + Q_p = \sqrt{\frac{16\pi}{5}}\left(\frac{3}{4\pi}AR^2\beta_2\right). \tag{5}$$

The root-mean-square (rms) matter radius is defined as

$$\langle r_m^2\rangle = \frac{1}{A}\int \rho(r_\perp, z)r^2 d\tau, \tag{6}$$

where A is the mass number, and $\rho(r_\perp, z)$ is the axially deformed density. We obtain the potentials, nucleon densities, single-particle energy levels, nuclear radii, quadrupole deformations, and the binding energies for a given nucleus. Converged ground states along with various constrained solutions can be obtained at different deformations including the fission state of a nucleus (see the potential energy surface).

To deal with the nuclear bulk properties of open-shell nuclei, one has to consider the pairing correlations [80]. There are various methods such as the BCS approach, the Bogoliubov transformation, and the particle number conserving methods that have been developed to treat the pairing effects in the study of nuclear properties including fission barriers [81–83]. The Bogoliubov transformation is a widely used method to take pairing correlation into account for the drip-line region [63–65,84]. In the case of nuclei not too far from the β-stability line, the constant gap BCS pairing approach provides a reasonably good description of pairing [85]. The present analysis is based on the superheavy mass nuclei around the β-stability line, hence the relativistic mean field results with BCS treatment should be applicable. Further, to avoid difficulties in the calculations, we have employed the constant gap BCS approach to deal with the present mass region [34,61,86–88].

III. CALCULATIONS AND RESULTS

In the relativistic mean field model, we perform the self-consistent calculations for a maximum boson major shell number $N_B = 20$ and varying maximum nucleon major shell number N_F from 14 to 24, to verify the convergence of the solutions by taking different inputs of initial deformation β_0 for the ground state [61,69,75,76]. From the results obtained, we found that the relative variations of the ground-state solutions are $\leqslant$0.004% for the binding energy and 0.002% for the nuclear radius. In the case of fission state solutions, the binding energy and nuclear radius vary $\leqslant$0.01% and 0.006%, respectively, over the range of major shell fermion number N_F from 16 to 28 for $N_B = 24$. Further, the quadrupole deformation in the fission states also varies up to $\leqslant$0.4% with fermion major shell number from 16 to 28 with fixed

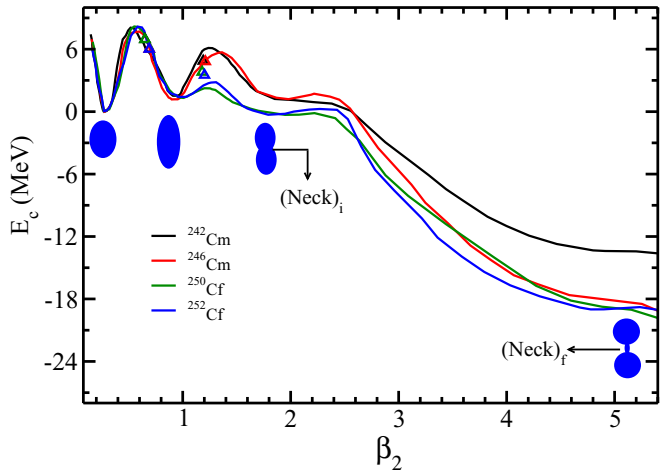

FIG. 1. The RMF (NL3*) potential energy surfaces of ^{242,248}Cm and ^{248,252}Cf as a function of the quadrupole deformation parameter β_2 are displayed with the empirical values [96] for the first and second barrier heights. The schematic diagram is given for a better visualization of the relative change in the shape with deformation. Heights are in MeV. See text for details.

$N_B = 24$. This implies that we can fix the number of major shells for fermions and bosons at $N_F = N_B = 20$ and $N_F = N_B = 24$ for the ground state and for the fission state of the considered mass region, respectively. The number of mesh points for Gauss-Hermite and Gauss-Lagurre integral are 20 and 24, respectively. We have used the recently developed NL3* interaction [69] for the present analysis, which is a version of the NL3 interaction [76] refitted to improve the description for the properties of neutron- and/or proton-rich exotic and superheavy nuclei [30,61,69].

For a given nucleus, we find various constrained solutions, including the fission state along with the ground state (see the potential curve Fig. 1). The calculated bulk properties such as binding energy (BE), root-mean-square (rms) charge radius, and qudrupole deformation β_2 for the ground state, first, second, third constrained and fission solutions are given in the first, second, third, and fourth rows for a given nucleus, respectively. The results obtained from the NL3* parameter set listed together with the predictions from the finite-range-droplet model (FRDM) [89,90], Hartree-Fock + BCS (HFBCS) [91], and the experimental data [92–94]. Because BE values are not available for HFBCS predictions, we have listed the rms charge radius r_{ch}, and the quadrupole deformation β_2 for comparison. All the isotopes of Cm and Cf are shown to have several intrinsic minima, where each minimum corresponds to a particular quadrupole deformation. For example, the ground state (g.s.), first, second minima (excited state), and the fission state deformation β_2 for ^{242}Cm are 0.287, 0.969, 2.113, and 5.036 of corresponding binding energy 1823.92 (*1823.3*), 1822.82, 1822.41, and 1837.38, respectively. Similarly, the values of β_2 for ^{248}Cf are 0.290 (*0.2972* ±0.019), 0.916, 2.161, and 4.936, with corresponding binding energy 1860.63 (*1859.2*), 1859.31, 1858.89, and 1881.18, respectively. Here the values in the bracket are the experimental ones. From Table I, one notices that the ground-state binding energies, charge radii, and β_2 values agree reasonably well with the available experimental data [92–94] and other theoretical predictions [89–91].

A. Potential energy surface

The potential energy surface (PES) is calculated by using the relativistic mean field formalism in a constrained procedure [30,33,34,43,61,80,95], i.e., instead of minimizing the H_0, we have minimized $H' = H_0 - \lambda Q_2$. Here, λ is a Lagrange multiplier and Q_2, the quadrupole moment. The term H_0 is the Dirac mean field Hamiltonian for the RMF model (the notations are standard and its form can be seen in Refs. [34,75]). In other words, we obtain the constrained solution from the minimization of $\sum_{ij} \frac{\langle\psi_i|H_0-\lambda Q_2|\psi_j\rangle}{\langle\psi_i|\psi_j\rangle}$ and calculate the constrained binding energy using H_0. The free energy is obtained from the minimization of $\sum_{ij} \frac{\langle\psi_i|H_0|\psi_j\rangle}{\langle\psi_i|\psi_j\rangle}$ and the converged energy solution does not depend on the initial guess value of the basis deformation β_0 as long as it is close to the minimum in the PES. However, it can converge to some other local minimum when β_0 is drastically different, and in this way we evaluate the different intrinsic isomeric states for a given nucleus. Note that the reflection symmetry is assumed for the calculation of the potential energy surface of the even-even isotopes of the Cm and Cf nuclei considered.

The potential energy surface for ^{242,246}Cm and ^{250,252}Cf nuclei are shown in Fig. 1 for a wide range of β_2 starting from the spherical to the hyperdeformed prolate configuration. The open triangle symbols in each PESs represented the empirical values [96] of the first and second barrier heights of the nucleus. Here, we find a multiminima structure in the PES for each isotope. The schematic diagram is given at or near each minimum of the figure for a better visualization of the relative changes in the shape of the nucleus with deformation. In Fig. 1, we have shown the PES's of ^{242,246}Cm and ^{250,252}Cf as a representative case. From the figure, one can notice that two identical major minima exist at $\beta_2 \approx 0.287$ and 0.969 for ^{242}Cm nuclei (see black line curve of Fig. 1 and Table I). Identical minima also appear in the case of all other isotopes of Cm and Cf nuclei at or near $\beta_2 \approx 0.28$ and 0.95, respectively. The calculated first and second barrier heights for all the isotopes along with the empirical values [96] are listed in Table II. The quadrupole deformation parameters and the barrier heights obtained from our calculations reasonably agree with the empirical values [93,96] of the isotopic chains of Cm and Cf nuclei for the first and second barriers, wherever available. For example, the obtained first and second barrier heights for ^{242}Cm are 7.92 and 5.76 MeV, respectively (see Table II). Similarly, the values are 8.06 and 2.83 MeV, respectively, for ^{250}Cf (see Table II). The corresponding empirical values for the first and second barrier height for ^{242}Cm and ^{250}Cf are 6.65 and 5.10 MeV and 5.60 and 3.80 MeV, respectively. Moreover, the calculated minima and/or the barriers in the PES shift a bit towards larger values of deformation β_2 in the isotopic chains.

The most important part of the PES is the path followed by the fission fragments. Following the PESs, we find an elongate fission path with conserved reflection symmetry for

TABLE I. The RMF (NL3*) results for the binding energy (BE), root-mean-square charge radius r_{ch} and the quadrupole deformation parameter β_2 for ^{242,244,246,248}Cm and ^{248,250,252,254}Cf nuclei. The ground state, and the constrained minima for the first, second, and fission states are given in the first, second, third, and fourth rows, respectively, for each nucleus. The finite-range-droplet model (FRDM) [89,90], Hartree-Fock + BCS (HFBCS) [91], and the experimental data [92–94] for the ground-state configurations are given for comparison, wherever available. The energies are in MeV and radii in fm.

	Binding energy			Charge radius			Quadrupole deformation			
Nucleus	RMF	Expt. [92]	FRDM [89]	RMF	Expt. [93]	HFBCS [91]	RMF	Expt. [94]	FRDM [90]	HFBCS [91]
^{242}Cm	1823.92	1823.3	1823.05	5.933	5.8285	5.90	0.287	–	0.224	0.25
	1822.82			6.560			0.969			
	1822.41			8.069			2.113			
	1837.38			11.016			5.036			
^{244}Cm	1836.24	1835.8	1835.79	5.946	5.8429	5.91	0.293	0.2972(17)	0.234	0.25
	1835.12			6.554			0.959			
	1834.89			8.445			2.071			
	1854.45			11.056			5.003			
^{246}Cm	1847.34	1847.8	1847.86	5.947	5.8475	5.93	0.293	0.2983(19)	0.234	0.27
	1845.75			6.553			0.921			
	1845.03			8.398			2.103			
	1866.02			10.986			4.987			
^{248}Cm	1860.63	1859.2	1859.28	5.959	5.8562	5.94	0.290	0.2972(19)	0.235	0.28
	1859.31			6.556			0.916			
	1858.89			8.501			2.161			
	1881.18			10.931			4.936			
^{248}Cf	1861.11	1857.8	1857.82	5.990	–	5.95	0.288	–	0.235	0.25
	1859.83			6.624			0.969			
	1861.43			8.554			2.149			
	1878.40			11.115			5.013			
^{250}Cf	1872.90	1870.0	1870.29	6.001	–	5.96	0.285	0.299(15)	0.245	0.28
	1871.81			6.641			0.967			
	1873.16			8.568			2.116			
	1892.03			11.076			5.007			
^{252}Cf	1883.82	1881.3	1881.32	6.011	–	5.97	0.278	–	0.236	0.25
	1882.64			6.681			1.081			
	1884.19			8.573			2.165			
	1902.66			11.002			4.984			
^{254}Cf	1893.25	1892.2	1891.69	6.022	–	5.97	0.272	–	0.226	0.24
	1891.96			6.987			1.083			
	1894.01			8.593			2.234			
	1812.51			10.926			4.912			

all the considered isotopes of Cm and Cf nuclei. After passing through the second barrier, at $\beta_2 \approx 2.15$, a lengthened double

TABLE II. The RMF (NL3*) results for the first and second barrier heights of even-even isotopes of Cm and Cf nuclei are compared with the empirical values (Emp.) [96]. Heights are in MeV.

	First barrier		Second barrier	
Nucleus	RMF	Emp. [96]	RMF	Emp. [96]
^{242}Cm	7.92	6.65	5.76	5.10
^{244}Cm	7.75	6.18	5.17	5.00
^{246}Cm	7.13	6.00	5.00	4.80
^{248}Cm	6.84	5.80	4.93	4.80
^{248}Cf	8.13	–	3.33	–
^{250}Cf	8.06	5.60	2.83	3.80
^{252}Cf	7.98	5.30	2.53	3.50
^{254}Cf	7.56	–	1.79	–

spherical structure with a very thick neck is visible in the density distribution, as shown in Fig. 2 (third panel), which is the hyperdeformed pre-fission state and will be discussed in the next subsection. In this range, the other shape degrees of freedom such as the octupole β_3 and/or hexadecapole deformation β_4 plays partial role in defining the fission path [97–99]. In other words, the slope of the fission path follow a shortened and/or lengthened valley partially depending on the shape degrees of freedom. In the present calculation, we have taken the reflectional symmetry, which elongates the fission path and for which the quadrupole deformation reach huge value $\beta_2 \approx 5.0$ with a pronounced neck configuration [presented as $(\text{Neck})_f$ in Fig. 1]. In other words, a very smooth hyperdeformed solution $(\text{Neck})_i$ preceded the fission configuration $(\text{Neck})_f$ with a large value of β_2. It is worth mentioning that the elongated valley does not have any special role in the fission fragments and neck constituents [33,97]. The aim of the present study to determine the neck configurations

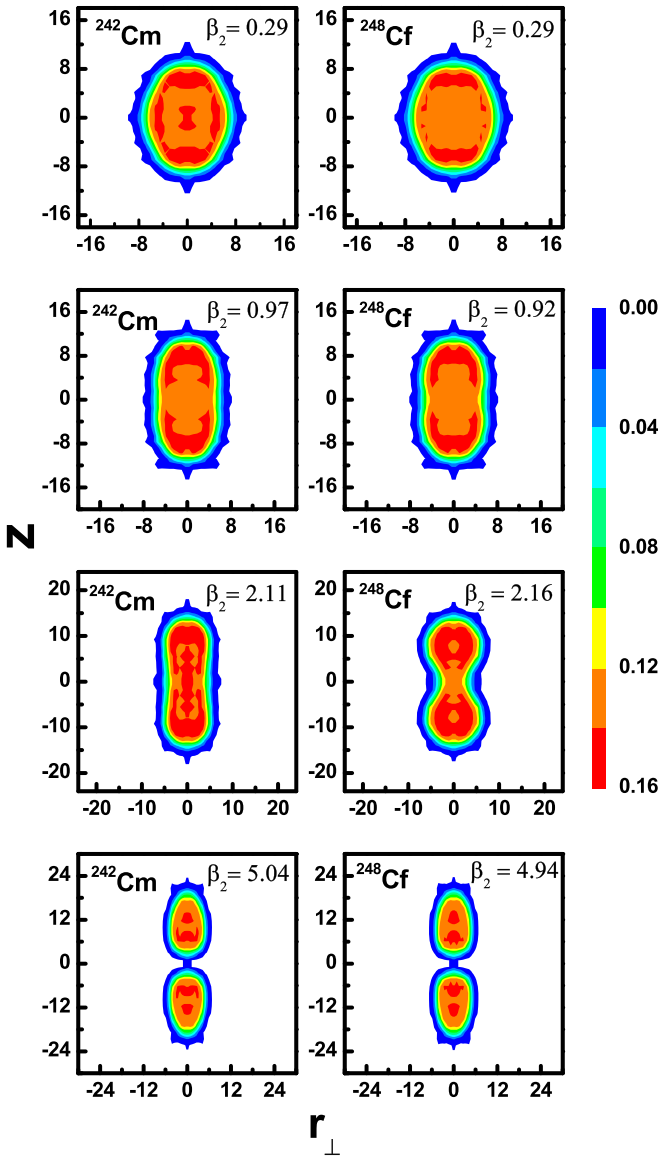

FIG. 2. The evolution of the static fission path for the isotopes of ^{242}Cm (left) and ^{248}Cf (right) as a function of quadrupole deformation β_2, corresponding to the possible minima obtained in the RMF formalism using the NL3* force parameter set. See text for details.

and identification of the neck constituents, which are almost independent of the intermediate valley followed by fissioning nuclei after the third barrier (see Fig. 1).

B. Nuclear shape with deformation

The present calculations mainly explain the nuclear structure and substructure of the nucleus, which depend on the density distributions of the protons and neutrons for each corresponding state. The density distribution of the nucleus is influenced by the nuclear deformations, which play a prominent role in the fission study. Here, we calculate the densities for the positive quadrant of the plane parallel to the z axis (i.e., the symmetry axis) and evaluated in the $zr_\perp$ plane, where $x^2 + y^2 = r_\perp^2$. The space reflection symmetries about both the z and $r_\perp$ axes are conserved in our formalism. The results for the density in the positive quadrant can be reflected in the other quadrants to get a complete picture of the nucleus in the $zr_\perp$ plane. The unbroken space reflection symmetries of our numerical procedure eliminate the odd multipoles (octupole, etc.) shape degrees of freedom. In other words, there are limitations in explaining nuclei with an asymmetric partition of particles that will not be properly clustered in the asymptotic limit. Nevertheless, the present study demonstrates the applicability of the RMF for studying the nuclear fission phenomenon and provides the scope for understanding the nuclear structure of even-even nuclei. Further, this furnishes an indication of the nuclear structure and substructures for various deformed states including the fission state. The present calculations are performed in an axially deformed coordinate space. Consideration of the deformed coordinate space might solve some of these issues and will throw more light on the substructure of the nuclei, which may be interesting work for the future.

In Fig. 2, we have presented typical examples for the matter density distributions of the ^{242}Cm and ^{248}Cf nuclei for all possible solutions, starting from the ground state up to the static fission configuration with a neck. The shape of the ^{242}Cm and ^{248}Cf nuclei follow the deformed ground-state solution around $\beta_2 \approx 0.29$, and the superdeformed and hyperdeformed prolate solutions obtained around $\beta_2 \approx 0.97$ and 2.35, respectively. Further, a well-defined dumbbell shape of the neck configuration is reproduced in the RMF study as a solution of the microscopic nuclear many-body Hamiltonian around $\beta_2 \approx 4.50$, in agreement with the age-old classical liquid drop picture of the fission process. The physical characteristics of the neck structures for the isotopic chain of Cm and Cf systems emerging from this study will be discussed later. From Fig. 2, the internal configurations for ^{242}Cm and ^{248}Cf nuclei are quite evident and similar structures can found for all the considered isotopes of Cm and Cf. The color code starts from deep red for maximum density distribution to blue representing the minimum density. One can analyze the distribution of nucleons inside the various isotopes at various shapes (in black and white figures, the color code is read as deep black with maximum density to light gray as minimum density distribution). The minimum density for the oblate state starts from 0.001 fm^{-3} and goes up to a maximum of 0.16 fm^{-3} for all the shapes (see Fig. 2). One notices that the central density ($\rho \approx 0.16$ fm^{-3}) becomes elongated with respect to deformation instead of changing in magnitude (see Table I and Fig. 2). Here, we also find the neck structures (i.e., the elongated shape with clear-cut neck before scission) similar to those of the microscopic study using the constrained method with Gogny interaction [100] and the Skyrme-Hartree-Fock model [101]. In other words, the fissioning systems energetically favor splitting into two separate fragments by developing an elongated shape with a neck.

Because our objective was to critically study the neck configurations, we have presented the matter density distributions for the fission states of our calculations for the four isotopes of Cm and Cf in Figs. 3 and 4, respectively. The binding energies, rms charge radii, and quadrupole deformations of the neck

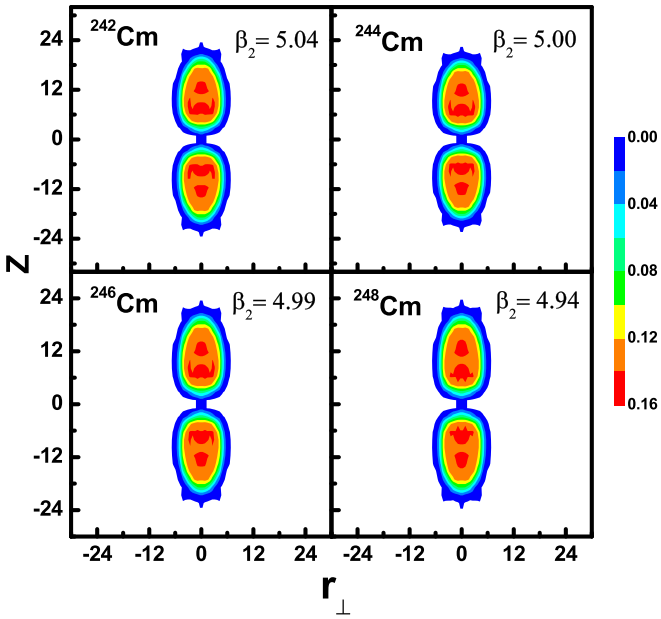

FIG. 3. The RMF (NL3*) total matter density distribution for the fission states of the ^{242,244,246,248}Cm nuclei. See text for details.

configuration for ^{242,244,246,248}Cm and ^{248,250,252,254}Cf can be seen in Table I. The calculated values for the first and second barrier heights are in reasonably good agreement with the empirical values [see Fig. 1 (open triangle) and Table II]. As can be seen in Fig. 1, the neck configurations lie ≈13 ± 4 MeV above the respective ground states in conformity with the expectation and in agreement with our general notion

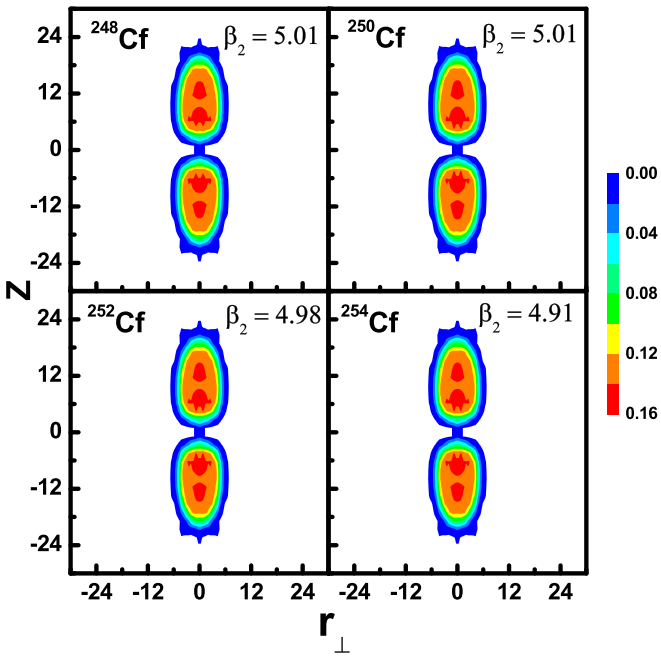

FIG. 4. The RMF (NL3*) total (neutron + proton) matter density distribution for the fission states of the ^{248,250,252,254}Cf nuclei. See text for details.

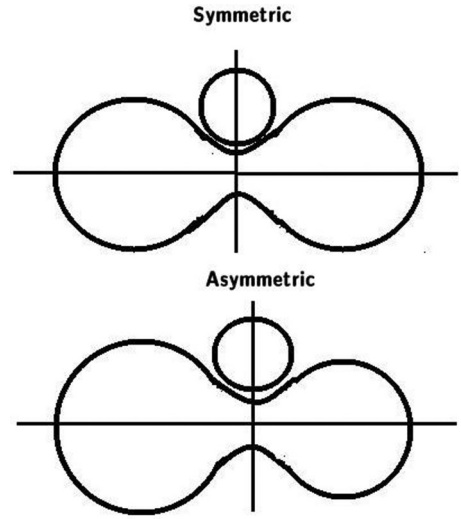

FIG. 5. The schematic diagram for the symmetric (top) and asymmetric (bottom) fission are given for a better visualization of neck structure. See text for details.

of fission dynamics. Further, the rms charge radii for the neck configurations are nearly twice those of the ground state, around 12 fm as expected. The path followed by the fissioning nuclei to reach the fission point is an elongated valley and final separation into two symmetric nuclei. This kind of fission is called elongated symmetric fission (SEF) [100]. In SEF, the quadrupole deformation reaches a sizable value with very low octopole deformation. As the present study is limited to quadrupole deformation with reflectional symmetry, in our case, this is the ultimate picture of the fission path. From Figs. 3 and 4, one notices the nucleus undergoing symmetric fission. The fission valley may slightly vary in the local minima after the second barrier on the β_3 and/or β_4 plane, but the most important ridge for the properties of neck structure and its constituents remain the same in the fission state.

C. Neck characteristics

The neck evolution is described in the traditional way by minimizing the Hartree energy under an external quadrupole moment constraint, $H' = H_0 - \lambda Q_2$ (defined above) of the system up to the scission point (shown in Figs. 3 and 4). From these figures, one can notice a sharp break of the liquid drop picture into two fragments with a well-defined neck structure within the microscopic relativistic mean field model for the NL3* parameter set. We now ask how the configuration (symmetric or asymmetric) of the fission fragments affect the neck constituents. As our study is limited to symmetric fission, in Fig. 5, we have given a schematic diagram for a better visualization of the fission fragments and neck configurations. The upper and lower parts of the diagram correspond to symmetric and asymmetric fission, respectively, along with neck evolution. From the schematic diagram, one can determine that the induced neck in the fission state is almost independent of the fission fragments. The area covered by the induced neck for symmetric fission balanced identically

TABLE III. The RMF (NL3*) characteristics of neck structure such as the quadrupole deformation (β_2), charge radius r_{ch}^{nk} of the fission state, average neutron ($\overline{\rho}_n^{nk}$) and proton density ($\overline{\rho}_p^{nk}$) and their ratio ($\frac{\overline{\rho}_n^{nk}}{\overline{\rho}_p^{nk}}$) in the neck region, dimension of the neck, length of the neck (L^{nk}), the number of neutron (N^{nk}) and proton (Z^{nk} of the neck for ^{242,244,246,248}Cm and ^{248,250,252,254}Cf are presented). See text for details.

Nucleus						Range						
β_2	r_{ch}^{nk}	$\overline{\rho}_n^{nk}$	$\overline{\rho}_p^{nk}$	$\frac{\overline{\rho}_n^{nk}}{\overline{\rho}_p^{nk}}$	$(r_1, r_2; z_1, z_2)$	L^{nk}	W^{nk}	N^{nk}	Z^{nk}	$\frac{N^{nk}}{Z^{nk}}$	Nucleus^{nk}	
^{242}Cm	5.036	11.089	0.032	0.035	0.91	±2.28; ±1.25	4.56	2.50	2.01	2.01	1.00	^{4}He
^{244}Cm	5.003	11.086	0.041	0.034	1.21	±2.28; ±1.25	4.56	2.50	2.09	2.05	1.02	^{4}He
^{246}Cm	4.987	10.982	0.047	0.033	1.42	±2.28; ±1.25	4.56	2.50	2.02	2.01	1.01	^{4}He
^{248}Cm	4.936	10.965	0.052	0.033	1.57	±2.28; ±1.25	4.56	2.50	2.06	2.01	1.02	^{4}He
^{248}Cf	5.013	11.115	0.034	0.037	0.92	±2.27; ±1.26	4.52	2.52	2.01	1.94	0.97	^{4}He
^{250}Cf	5.007	11.076	0.046	0.036	1.28	±2.27; ±1.26	4.52	2.52	2.05	1.98	0.95	^{4}He
^{252}Cf	4.984	10.972	0.051	0.035	1.46	±2.27; ±1.26	4.52	2.52	2.08	2.01	1.03	^{4}He
^{254}Cf	4.912	10.843	0.055	0.034	1.62	±2.27; ±1.26	4.52	2.52	2.09	2.01	1.04	^{4}He

to both the fragments, whereas in the case of asymmetric fission, the neck shifts towards the massive fragments instead of changing the neck structure. In other words, the area covered by the neck region for symmetric and asymmetric fission are almost identical. Hence, in the naked eye visualization, we can conclude that the neck constituents are a little dependent and/or independent of the fission fragments.

As mentioned above, here our main aim is to determine the neck constituents in the fission state. The calculated yields of the total number of neutrons N^{nk} and protons Z^{nk} contained in the neck are obtained by integrating the corresponding densities over the physical dimension of the neck. The number of nucleons for the neck regions can be calculated by

$$N^{nk} = \iint \rho_n^{nk}(r_\perp, z) d\tau, \tag{7}$$

and

$$Z^{nk} = \iint \rho_p^{nk}(r_\perp, z) d\tau, \tag{8}$$

where ρ_n^{nk} and ρ_p^{nk} are the calculated RMF neutron and proton density distributions of the nucleus in the neck configuration, respectively. We also present the mean neutron and proton densities of the neck as

$$\overline{\rho}_{n,p}^{nk} = \frac{\int \rho_{n,p}^{nk} d\tau}{\int d\tau}. \tag{9}$$

From Eq. (9), we estimate the average neutron $\overline{\rho}_n^{nk}$ and proton $\overline{\rho}_p^{nk}$ density and their ratio $\overline{\rho}_n^{nk}/\overline{\rho}_p^{nk}$ for the neck region. The estimates for the neutron and/or proton constituents and their asymmetry are listed in Table III for ^{242,244,246,248}Cm and ^{242,244,246,248}Cf nuclei. As expected, the $\overline{\rho}_n^{nk}$ and $\overline{\rho}_p^{nk}$ for both the elements remain similar for all isotopes, being around 0.035 fm^{-3} (see Table III). The $\overline{\rho}_n^{nk}$ for the isotopic chains of Cm and Cf nuclei, gradually increase with the neutron number. Furthermore, the neutron to proton density ratio $\overline{\rho}_n^{nk}/\overline{\rho}_p^{nk}$ increases gradually with respect to neutron number, as expected. In the isotopic chain of the Cm nuclei, the ratio has increased from 0.91 for ^{242}Cm to 1.57 for ^{248}Cm. The corresponding values are 0.92 for ^{248}Cf to 1.62 for ^{254}Cf (see Table III).

We have estimated the length of the neck in the fission state, which is quite important for determining the neck constituents. The length of the neck L^{nk} is the distance between the two facing connecting surfaces. The width of the neck is also quite important in determining the constituents, using Eqs. (7) and (8), because the total number of nucleon(s) is(are) nothing but the average out sum of the matter densities within the area cover by $L^{nk} \times W^{nk}$ (see Table III). The length of the neck L_n, width W^{nk}, and its constituents are listed in Table III. From Table III, one can find the charge radius is of the neck configuration for each the isotopes, which is about 12 fm with a well-defined neck and fairly extended mass distribution evident in all cases. It is indeed interesting that heavy and superheavy nuclei acquire such an extended dumbbell configuration, supported by the nucleon-nucleon force [39,102]. As we move from ^{242}Cm to ^{248}Cm, the number of neck neutron and neck proton numbers remain unchanged. A similar trend is seen for the Cf isotopes. It may be noticed that the magnitude of the ratio N^{nk}/Z^{nk} is somewhat different from that of the average neutron-to-proton neck densities $\overline{\rho}_n^{nk}/\overline{\rho}_p^{nk}$ (find in Table III). It shows that the effective volume distributions of neutrons and protons are different in the neck region. The ratio of neutron-to-proton number in the neck region found in our present calculation is about 1.0 ± 0.02 for all the isotopes of Cm and Cf nuclei. Hence the neck can be considered as a quasibound transient state of any $N = Z$ nucleus. Following the obtained values of neutrons and protons, the neck nucleus correlated with those transient state being ^{4}He (α particle) for ^{242,244,246,248}Cm and ^{248,250,252,254}Cf. This implies that the α particle is the evaporation residue for the considered isotopes of Cm and Cf nuclei. More detailed studies in this direction is highly welcome.

IV. SUMMARY AND CONCLUSIONS

In the present study, we have investigated the mechanism of fission decay and the shape of the nucleus by following the static fission path to the configuration before the breakup. The well-established microscopic many-body nuclear Hamiltonian, i.e., the RMF theory is employed for estimating the classical liquid-drop picture of the fission state. The actinide isotopes of Cm and Cf nuclei near the valley of stability

have been studied with the objective of relevance in stellar evolution. We found a deformed prolate configuration for the ground state of the isotopic chain for Cm and Cf nuclei. Furthermore, a highly deformed configuration with a neck is found by using a very large basis consisting of as many as 24 oscillator shells, while for the ground state 20 shells are adequate. This study has revealed the anatomy of the neck in the fission state, such as the average neutron-proton asymmetry, the length, and composition. We found that the average neutron-proton ratio of the neck region progressively increases with the neutron number in the isotopic chains of Cm and Cf nuclei. The neutron-to-proton number ratio found in our calculation is 1.0 ± 0.02, which may correlate with the quasbound and/or a resonance state of a light $N = Z$ nucleus and/or α particle. The necks found in the calculation at the above exotic nuclei suggest a point where along with the two heavy fragments, an α particle might be emitted at scission for the isotopes of Cm and Cf nuclei considered. The evolution of neck and the neutron-to-proton ratio of the neck constituents gives a probationary picture of the scission, where the parent nucleus breaks down into two fragments by emitting these light $N = Z$ nucleus and/or α particle. This would have an effective indication in the energy generation of *r*-process nucleosynthesis in stellar evolution.

ACKNOWLEDGMENTS

This work was supported by FAPESP Projects No. 2014/26195-5 and No. 2017/05660-0, INCT-FNA Project No. 464898/2014-5, and the CNPq–Brasil. M.B. thanks S.-G. Zhou for his many-fold discussions throughout the work.

[1] O. Hahn and F. Strassmann, Die Naturwissenschaften **27**, 11 (1939).
[2] L. Meitner and O. R. Fritsch, Nature (London) **143**, 239 (1939).
[3] N. Bohr and J. A. Wheeler, Phys. Rev. **56**, 426 (1939).
[4] S. Hofmann and G. Mũnzenberg, Rev. Mod. Phys. **72**, 733 (2000).
[5] Y. Oganessian, J. Phys. G: Nucl. Phys. **34**, R165 (2007).
[6] Y. T. Oganessian *et al.*, Phys. Rev. Lett. **104**, 142502 (2010).
[7] P. Mõller, A. J. Sierk, T. Ichikawa, A. Iwamoto, R. Bengtsson, H. Uhrenholt, and S. Aberg, Phys. Rev. C **79**, 064304 (2009).
[8] Z.-H. Liu and J.-D. Bao, Phys. Rev. C **84**, 031602(R) (2011).
[9] P. Mõller, D. G. Madland, A. J. Sierk, and A. Iwamoto, Nature (London) **409**, 785 (2001).
[10] A. Dobrowolski, K. Pomorski, and J. Bartel, Phys. Rev. C **75**, 024613 (2007).
[11] F. A. Ivanyuk and K. Pomorski, Phys. Rev. C **79**, 054327 (2009).
[12] M. Kowal, P. Jachimowicz, and A. Sobiczewski, Phys. Rev. C **82**, 014303 (2010).
[13] G. Royer, M. Jaffre, and D. Moreau, Phys. Rev. C **86**, 044326 (2012).
[14] C.-L. Zhong and T.-S. Fan, Commun. Theor. Phys. **62**, 405 (2014).
[15] A. Mamdouh, J. M. Pearson, M. Rayet, and F. Tondeur, Nucl. Phys. A **644**, 389 (1998).
[16] L. Ghys, A. N. Andreyev, S. Antalic, M. Huyse, and P. Van Duppen, Phys. Rev. C **91**, 044314 (2015).
[17] T. Burvenich, M. Bender, J. A. Maruhn, and P.-G. Reinhard, Phys. Rev. C **69**, 014307 (2004).
[18] S. Goriely, M. Samyn, and J. M. Pearson, Phys. Rev. C **75**, 064312 (2007).
[19] F. Minato, S. Chiba, and K. Hagino, Nucl. Phys. A **831**, 150 (2009).
[20] J. C. Pei, W. Nazarewicz, J. A. Sheikh, and A. K. Kerman, Phys. Rev. Lett. **102**, 192501 (2009).
[21] P. Goddard, P. Stevenson, and A. Rios, Phys. Rev. C **92**, 054610 (2015).
[22] Y. Zhu and J. C. Pei, Phys. Rev. C **94**, 024329 (2016).
[23] J. L. Egido and L. M. Robledo, Phys. Rev. Lett. **85**, 1198 (2000).
[24] M. Warda, K. Pomorski, J. L. Egido, and L. M. Robledo, J. Phys. G: Nucl. Part. Phys. **31**, S1555 (2005).
[25] M. Warda and J. L. Egido, Phys. Rev. C **86**, 014322 (2012).
[26] G. F. Bertsch, Int. J. Mod. Phys. E **26**, 1740001 (2017).
[27] M. Bender, P.-H. Heenen, and P.-G. Reinhard, Rev. Mod. Phys. **75**, 121 (2003).
[28] H.-F. Lũ, L.-S. Geng, and J. Meng, Chin. Phys. Lett. **23**, 2940 (2006).
[29] S. K. Patra, R. K. Choudhury, and L. Satpathy, J. Phys. G: Nucl. Part. Phys. **37**, 085103 (2010).
[30] M. Bhuyan. S. K. Patra, P. Arumugam, and Raj K. Gupta, Int. J. Mod. Phys. E **20**, 1227 (2011).
[31] B.-N. Lu, E.-G. Zhao, and S.-G. Zhou, Phys. Rev. C **85**, 011301(R) (2012).
[32] V. Prassa, T. Nikšić, and D. Vretenar, Phys. Rev. C **88**, 044324 (2013).
[33] B.-N. Lu, J. Zhao, E.-G. Zhao, and S.-G. Zhou, Phys. Rev. C **89**, 014323 (2014).
[34] M. Bhuyan, S. K. Patra, and Raj K. Gupta, J. Phys. G: Nucl. Part. Phys. **42**, 015105 (2015).
[35] N. Schunck and L. M. Robledo, Rep. Prog. Phys. **79**, 116301 (2016).
[36] M. Warda, J. L. Egido, L. M. Robledo, and K. Pomorski, Phys. Rev. C **66**, 014310 (2002).
[37] P. Madler, Z. Phys. A **321**, 343 (1985).
[38] M. S. Samant, R. P. Anand, R. K. Choudhury, S. S. Kapoor, and D. M. Nadkarni, Phys. Rev. C **51**, 3127 (1995).
[39] L. Satpathy, S. K. Patra, and R. K. Choudhury, PRAMANA - J. Phys. **70**, 87 (2008).
[40] A. Staszczak and Z. Łojewski, Nucl. Phys. A **657**, 134 (1999).
[41] J. F. Berger and K. Pomorski, Phys. Rev. Lett. **85**, 30 (2000).
[42] M. Warda, A. Staszczak, and W. Nazarewicz, Phys. Rev. C **86**, 024601 (2012).
[43] W. Koepf and P. Ring, Phys. Lett. B **212**, 397 (1988).
[44] J. Fink, V. Blum, P.-G. Reinhard, J. A. Maruhn, and W. Greiner, Phys. Lett. B **218**, 277 (1989).
[45] M. Leino, J. Ãystõ, T. Enqvist, P. Heikkinen, A. Jokinen, M. Nurmia, A. Ostrowski, W. H. Trzaska, J. Uusitalo, K. Eskola, P. Armbruster, and V. Ninov, Nucl. Instrum. Methods Phys. Res., Sect. B **99**, 653 (1995).
[46] C. J. Gross, T. N. Ginter, D. Shapira, W. T. Milner, J. W. McConnell, A. N. James, J. W. Johnson, J. Mas, P. F. Mantica,

R. L. Auble, J. J. Das, J. L. Blankenship *et al.*, Nucl. Instrum. Methods Phys. Res., Sect. A **450**, 12 (2000).
[47] Z. Sun, W. L. Zhan, Z. Y. Guo, G. Xiao, and J. X. Li, Nucl. Instrum. Methods Phys. Res., Sect. A **503**, 496 (2003).
[48] M. Winkler, H. Geissel, H. Weick, B. Achenbach, K.-H. Behr, D. Boutin, A. Brünle, M. Gleim, W. Hũller, C. Karagiannis, A. Kelic, B. Kindler *et al.*, Nucl. Instrum. Methods Phys. Res., Sect. B **266**, 4183 (2008).
[49] H. Sakurai, Nucl. Phys. A **805**, 526c (2008).
[50] A. C. Mueller and R. Anne, Nucl. Instrum. Methods Phys. Res., Sect. B **56**, 559 (1991).
[51] H. Geissel, P. Armbruster, K. H. Behr, A. Brũnle, K. Burkard, M. Chen, H. Folger, B. Franczak, H. Keller, O. Klepper, B. Langenbeck, F. Nickel *et al.*, Nucl. Instrum. Methods Phys. Res., Sect. B **70**, 286 (1992).
[52] A. M. Rodin, S. V. Stepantsov, D. D. Bogdanov, M. S. Golovkov, A. S. Fomichev, S. I. Sidorchuk, R. S. Slepnev, R. Wolski, G. M. Ter-Akopian, Y. T. Oganessian, A. A. Yukhimchuk, V. V. Perevozchikov *et al.*, Nucl. Instrum. Methods Phys. Res., Sect. B **204**, 114 (2003).
[53] M. Thoennessen, Nucl. Phys. A **834**, 688c (2010).
[54] S. Goriely, A. Bauswein, and H. T. Janka, Ast. Phys. J. **738**, L32 (2011).
[55] O. Korobkin, S. Rosswog, A. Arcones, and C. Winteler, Mon. Not. R. Astron. Soc. **426**, 1940 (2012).
[56] O. Just, A. Bauswein, R. A. Pulpillo, S. Goriely, and H.-T. Janka, Mon. Not. R. Astron. Soc. **448**, 541 (2015).
[57] J. Boguta and A. R. Bodmer, Nucl. Phys. A **292**, 413 (1977).
[58] B. D. Serot and J. D. Walecka, in *Advances in Nuclear Physics*, Vol. 16, edited by J. W. Negele and E. Vogt (Plenum Press, New York, 1986), p. 1.
[59] W. Pannert, P. Ring, and J. Boguta, Phys. Rev. Lett. **59**, 2420 (1987).
[60] G. A. Lalazissis, S. Raman, and P. Ring, At. Data Nucl. Data Tables **71**, 1 (1999).
[61] S. K. Patra, M. Bhuyan, M. S. Mehta, and R. K. Gupta, Phys. Rev. C **80**, 034312 (2009).
[62] P.-G. Reinhard, Rep. Prog. Phys. **52**, 439 (1989).
[63] P. Ring, Prog. Part. Nucl. Phys. **37**, 193 (1996).
[64] D. Vretenar, A. V. Afanasjev, G. A. Lalazissis, and P. Ring, Phys. Rep. **409**, 101 (2005).
[65] J. Meng, H. Toki, S. G. Zhou, S. Q. Zhang, W. H. Long, and L. S. Geng, Prog. Part. Nucl. Phys. **57**, 470 (2006).
[66] T. Nikšić, D. Vretenar, and P. Ring, Prog. Part. Nucl. Phys. **66**, 519 (2011).
[67] D. Logoteta, I. Vidaña, C. Providência, A. Polls, and I. Bombaci, J. Phys. Conf. Ser. **342**, 012006 (2012).
[68] X.-F. Zhao and H.-Y. Jia, Phys. Rev. C **85**, 065806 (2012).
[69] G. A. Lalazissis, S. Karatzikos, R. Fossion, D. Pena Arteaga, A. V. Afanasjev, and P. Ring, Phys. Lett. B **671**, 36 (2009).
[70] B. A. Nikolaus, T. Hoch, and D. G. Madland, Phys. Rev. C **46**, 1757 (1992).
[71] T. Burvenich, D. G. Madland, J. A. Maruhn, and P.-G. Reinhard, Phys. Rev. C **65**, 044308 (2002).
[72] C. Fuchs, H. Lenske, and H. H. Wolter, Phys. Rev. C **52**, 3043 (1995).
[73] T. Niksic, D. Vretenar, P. Finelli, and P. Ring, Phys. Rev. C **66**, 024306 (2002).
[74] R. Brockmann and H. Toki, Phys. Rev. Lett. **68**, 3408 (1992).
[75] Y. K. Gambhir, P. Ring, and A. Thimet, Ann. Phys. (NY) **198**, 132 (1990).
[76] G. A. Lalazissis, J. König, and P. Ring, Phys. Rev. C **55**, 540 (1997).
[77] C. J. Horowitz and B. D. Serot, Nucl. Phys. A **368**, 503 (1981).
[78] J. Boguta, Nucl. Phys. A **372**, 386 (1981).
[79] C. E. Price and G. E. Walker, Phys. Rev. C **36**, 354 (1987).
[80] S. Karatzikos, A. V. Afanasjev, G. A. Lalazissis, and P. Ring, Phys. Lett. B **689**, 72 (2010).
[81] J. Y. Zeng and T. S. Cheng, Nucl. Phys. A **405**, 1 (1983).
[82] H. Molique and J. Dudek, Phys. Rev. C **56**, 1795 (1997).
[83] T. V. Nhan Hao, P. Quentin, and L. Bonneau, Phys. Rev. C **86**, 064307 (2012).
[84] G. A. Lalazissis, D. Vretenar, P. Ring, M. Stoitsov, and L. M. Robledo, Phys. Rev. C **60**, 014310 (1999).
[85] J. Dobaczewski, H. Flocard, and J. Treiner, Nucl. Phys. A **422**, 103 (1984).
[86] D. G. Madland and J. R. Nix, Nucl. Phys. A **476**, 1 (1981).
[87] P. Möller and J. R. Nix, At. Data Nucl. Data Tables **39**, 213 (1988).
[88] M. Bhuyan, B. V. Carlson, S. K. Patra, and S.-G. Zhou, Phys. Rev. C **97**, 024322 (2018).
[89] P. Möller, J. R. Nix, W. D. Myers, and W. J. Swiatecki, At. Nucl. Data Tables **59**, 185 (1995).
[90] P. Möller, J. R. Nix, and K.-L. Kratz, At. Data Nucl. Data Tables **66**, 131 (1997).
[91] S. Goriely, F. Tondeur, and J. M. Pearson, At. Data Nucl. Data Tables **77**, 311 (2001).
[92] M. Wang, G. Audi, A. H. Wapstra, F. G. Kondev, M. MacCormick, X. Xu, and B. Pfeier, Chin. Phys. C **36**, 1603 (2013).
[93] I. Angeli and K. P. Marinova, At. Data Nucl. Data Tables **99**, 69 (2013).
[94] S. Raman, C. W. Nestor, Jr., and P. Tikkanen, At. Data Nucl. Data Tables **78**, 1 (2001).
[95] H. Flocard, P. Quentin, and D. Vautherin, Phys. Lett. B **46**, 304 (1973).
[96] R. Capote, M. Herman, P. Oblozinsky, P. Young, S. Goriely, T. Belgya, A. Ignatyuk, A. Koning, S. Hilaire, V. Plujko, M. Avrigeanu, O. Bersillon, M. Chadwick, T. Fukahori, Z. Ge, Y. Han, S. Kailas, J. Kopecky, V. Maslov, G. Reffo, M. Sin, E. Soukhovitskii, and P. Talou, Special Issue on Nuclear Reaction Data, Nucl. Data Sheets **110**, 3107 (2009).
[97] P. Mõller, A. J. Sierk, and A. Iwamoto, Phys. Rev. Lett. **92**, 072501 (2004).
[98] S. E. Agbemava, A. V. Afanasjev, D. Ray, and P. Ring, Phys. Rev. C **95**, 054324 (2017).
[99] J. Zhao, T. Nikšić, D. Vretenar, and S.-G. Zhou, Phys. Rev. C **99**, 014618 (2019).
[100] N. Dubray, H. Goutte, and J.-P. Delaroche, Phys. Rev. C **77**, 014310 (2008).
[101] L. Bonneau, Phys. Rev. C **74**, 014301 (2006).
[102] D. M. Brink, *International School of Physics Enrico Fermi*, Course 36 (Academic, Berlin, 1996).